Berry phase of nonideal Dirac fermions in topological insulators

A. A. Taskin and Yoichi Ando
Institute of Scientific and Industrial Research, Osaka University, Ibaraki, Osaka 567-0047, Japan
(Received 16 March 2011; revised manuscript received 27 April 2011; published 12 July 2011)

A distinguishing feature of Dirac fermions is the Berry phase of π associated with their cyclotron motions. Since this Berry phase can be experimentally assessed by analyzing the Landau-level fan diagram of the Shubnikov–de Haas (SdH) oscillations, such an analysis has been widely employed in recent transport studies of topological insulators to elucidate the Dirac nature of the surface states. However, the reported results have usually been unconvincing. Here we show a general scheme for describing the phase factor of the SdH oscillations in realistic surface states of topological insulators, and demonstrate how one can elucidate the Dirac nature in real experimental data.

DOI: 10.1103/PhysRevB.84.035301 PACS number(s): 73.25.+i, 73.20.At, 71.70.Di, 72.20.My

I. INTRODUCTION

During the last three decades, the Berry phase[1] has become an important concept in condensed matter physics,[2] playing a fundamental role in various phenomena such as electric polarization,[3] orbital magnetism,[4,5] anomalous Hall effects,[6] etc. The Berry phase (or geometrical phase) in solids[7] is determined by topological characteristics of the energy bands in the Brillouin zone (BZ) and represents a fundamental property of the system.[8] For example, a nonzero Berry phase, which can be measured directly in magnetotransport experiments, reflects the existence of a singularity in the energy bands such as a band-contact line in three-dimensional (3D) bulk states or a Dirac point in a two-dimensional (2D) surface state.[9] Also, the Berry phase of π is responsible for the peculiar "antilocalization" effects in carbon nanotubes or graphene.[10] Recently, the π Berry phase has been observed in the Shubnikov–de Haas (SdH) oscillations in graphene,[11,12] giving one of the key pieces of evidence for the Dirac nature of quasiparticles in the 2D carbon sheet.

The 3D topological insulator[13–16] (TI) also supports spin-polarized 2D Dirac fermions on its surface,[17] which can be distinguished from ordinary charge carriers by a nonzero Berry phase. Recently, several groups have reported observations of the SdH oscillations coming from the 2D surface states of TIs.[18–25] In those studies, a finite Berry phase has been reported, but it usually deviates from the exact π value. For example, in the new TI material Bi_2Te_2Se (BTS),[21] where a large contribution of the surface transport to the total conductivity has been observed, the apparent Berry phase extracted from the SdH-oscillation data was 0.44π. So far, the Zeeman coupling of the spin to the magnetic field has been considered[20] as a possible source of such a discrepancy. Here, we show that in addition to the Zeeman term, the deviation of the dispersion relation $E(k)$ from an ideal linear dispersion[26] can shift the Berry phase from π. We further show how the real experimental data for nonideal Dirac fermions can be understood by taking into account those additional factors.

II. ENERGY DISPERSION OF SURFACE STATES

The energy dispersion of the surface states in TIs can be directly measured in angle-resolved photoemission spectroscopy (ARPES) experiments. As an example, Fig. 1 shows the dispersion of the surface state (together with the bulk state) in BTS reported by Xu *et al.*[27] One can easily recognize that $E(k)$ is not an ideal Dirac-like dispersion, but it can be fitted reasonably well for the two high-symmetry axes with

$$E(k) = v_F \hbar k + \frac{\hbar^2}{2m} k^2, \tag{1}$$

with a single Fermi velocity $v_F = 3.4\times10^5$ m/s and an effective mass m which slightly varies with the direction in the surface BZ as shown by the solid lines in Fig. 1 [$m/m_0 =$ 0.15 (0.125) for the $\bar{\Gamma} \to \bar{M}$ ($\bar{\Gamma} \to \bar{K}$) direction with m_0 the free-electron mass].

Similar fittings can be obtained for other TIs owing to the progress in ARPES studies of these materials.[17,24,28,29]

III. BERRY PHASE IN QUANTUM OSCILLATIONS

It is commonly accepted that quantum oscillations observed in 3D metals can be well understood within Lifshits-Kosevich[30] (the de Haas–van Alphen effect) and Adams-Holstein[31] (the SdH effect) theories. Recently this approach has been generalized to describe magnetic oscillations in graphene, which is a 2D system with a Dirac-like spectrum of charge carriers.[32,33] There are two most prominent features that distinguish such systems from materials with a parabolic spectrum: First, rather weak magnetic fields are sufficient to bring the system into a regime where only a few Landau levels are occupied. Second, Dirac quasiparticles acquire the Berry phase of π in the cyclotron motion, changing the phase of quantum oscillations.

In the SdH effect, the oscillating part of ρ_{xx} follows

$$\Delta\rho_{xx} \sim \cos\left[2\pi\left(\frac{F}{B} - \gamma\right)\right], \tag{2}$$

where F is the oscillation frequency and $2\pi\gamma$ is the phase factor ($0 \leqslant \gamma < 1$). This is the same γ as in the Onsager semiclassical quantization condition[34]

$$A_N = \frac{2\pi e}{\hbar} B(N + \gamma), \tag{3}$$

when the Nth Landau level (LL) is crossing the Fermi energy E_F (A_N is the area of an electron orbit in the k space). γ is

 ©2011 American Physical Society

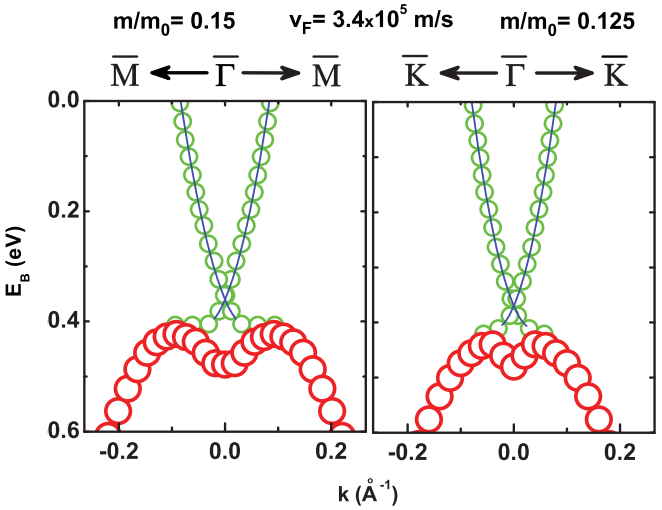

FIG. 1. (Color online) Experimental band dispersions (symbols) in Bi_2Te_2Se measured by ARPES in Ref. 27 and the fitting of Eq. (1) to the surface state (solid line). Large symbols depict the bulk state.

directly related to the Berry phase through[9]

$$\gamma - \frac{1}{2} = -\frac{1}{2\pi}\oint_{\Gamma} \vec{\Omega}\, d\vec{k}, \tag{4}$$

where $\vec{\Omega}(\vec{k}) = i\int d\vec{k}\, u^*_{\vec{k}}(\vec{r})\,\vec{\nabla}_{\vec{k}} u_{\vec{k}}(\vec{r})$ is the Berry connection, $u_{\vec{k}}(\vec{r})$ is the amplitude of the Bloch wave function, and Γ is a closed electron orbit [the intersection of the Fermi surface $E(\vec{k}) = E_F$ with the plane $k_z = \text{const}$]. For spinless quasiparticles, it is known[9,34] that the Berry phase is zero for a parabolic energy dispersion ($\gamma = \frac{1}{2}$) and π for a linear energy dispersion ($\gamma = 0$).

Experimentally, γ can be obtained from an analysis of the Landau-level fan diagram. There are three quantities which are often used as abscissa for plotting a LL fan diagram: (i) The Landau level index N, which determines the energy E_N of the Nth LL. (ii) The filling factor ν ($\equiv \frac{N_s S}{N_\phi}$, where N_s is the density of charge carriers, S is the area of the sample, $N_\phi = \frac{BS}{\Phi_0}$ is the number of flux quanta, and $\Phi_0 = \frac{h}{e}$ is the flux quantum). (iii) An integer number n which marks the nth minimum of the oscillations in ρ_{xx}. Although all three quantities are related to each other, the most straightforward way to plot a LL fan diagram from the ρ_{xx} oscillations in a 2D system[18] is to assign an integer n to a minimum of ρ_{xx} (or a half integer to a maximum of ρ_{xx}). From Eq. (2), one can see that the first minimum in ρ_{xx} is always in the range of $0 < \frac{F}{B_1} \leqslant 1$. Thus, the plot of F/B_n vs n, which makes a straight line with a unit slope for periodic oscillations, is uniquely defined and cuts the n axis between 0 and 1 depending on the phase of the oscillations, γ.

The ordinate $1/B_n$ in a LL fan diagram is determined by the Landau quantization of the cyclotron motion of electrons in a magnetic field. In 2D systems, upon sweeping B, ρ_{xx} shows a maximum (or a sharp peak in the quantum Hall effect[18]) each time that $E_N(B)$ crosses the Fermi level. Thus, the position of the maximum in ρ_{xx} that corresponds to the N th LL, $1/B_N$, is given by

$$2\pi\left(\frac{F}{B_N} - \gamma\right) = 2\pi N. \tag{5}$$

On the other hand, the n th minimum in ρ_{xx} occurs at $1/B_n$ when $2\pi(\frac{F}{B_n} - \gamma) = 2\pi n - \pi$, so the positions of the maxima and minima are shifted by $\frac{1}{2}$ on the n axis.

The Onsager relation[34] gives F in terms of the Fermi wave vector k_F as $F = (\hbar/2\pi e)\pi k_F^2$, and this k_F can be calculated from Eq. (1) as

$$k_F^2 = 2\left(\frac{mv_F}{\hbar}\right)^2\left(1 + \frac{E_F}{mv_F^2} - \sqrt{1 + \frac{2E_F}{mv_F^2}}\right). \tag{6}$$

Also, when E_F is at the N th LL, there is a relation

$$E_N(B_N) = E_F. \tag{7}$$

From Eqs. (5)–(7), one obtains

$$\gamma = \frac{mv_F^2}{\hbar\,\omega_c}\left(1 + \frac{E_N}{mv_F^2} - \sqrt{1 + \frac{2E_N}{mv_F^2}}\right) - N, \tag{8}$$

where $\omega_c = eB/m$ is the cyclotron frequency.

In the general case, γ is a function of B, meaning that oscillations in ρ_{xx} are quasiperiodic in $1/B$. In order to calculate γ one needs to find the eigenvalues E_N for a given Hamiltonian.

IV. MODEL HAMILTONIAN

For the (111) surface state of the Bi_2Se_3-family TI compounds, the Hamiltonian for nonideal Dirac quasiparticles in perpendicular magnetic fields can be written as[35]

$$\hat{H} = v_F(\Pi_x\sigma_y - \Pi_y\sigma_x) + \frac{\Pi^2}{2m} - \frac{1}{2}\,g_s\mu_B B\sigma_z, \tag{9}$$

where the Landau gauge $\mathbf{A} = (0, By, 0)$ for the vector potential is used, $\Pi = \hbar\mathbf{k} + e\mathbf{A}$, σ_i are the Pauli matrices, μ_B is the Bohr magneton, and g_s is the surface g-factor. Note that this Hamiltonian is essentially the same as for a conventional 2D electron gas (2DEG) with Bychkov-Rashba spin-orbit interaction term.[36] The only difference is that in TIs the parabolic term in Eq. (1) is a small perturbation in comparison with the linear one. The LL energies are given by[35–37]

$$E_N^{(\pm)} = \hbar\omega_c N \pm \sqrt{2\hbar\, v_F^2 eBN + \left(\frac{1}{2}\hbar\omega_c - \frac{1}{2}\,g_s\mu_B B\right)^2}, \tag{10}$$

where the "+" and "−" branches are for electrons and holes, respectively. The obtained eigenvalues E_N define the exact positions of maxima in ρ_{xx} and, thus, the phase of oscillations through Eq. (8).

In two extreme cases, for nonmagnetic fermions ($g_s = 0$), Eq. (8) gives the expected results. First, for a linear dispersion (ideal Dirac fermions), $m \to \infty$ leads to $E_N = \pm\sqrt{2\hbar\, ev_F^2 BN}$ and $\gamma \to \frac{E_N^2}{2\hbar\, ev_F^2 B} - N$, giving $\gamma = 0$ (Berry phase is π). Second, for a parabolic dispersion, $v_F \to 0$ leads to $E_N = \hbar\,\omega_c(N + \frac{1}{2})$ and $\gamma \to \frac{E_N}{\hbar\,\omega_c} - N$, giving $\gamma = \frac{1}{2}$ (Berry phase is zero). This gives confidence that the expression for γ given

in Eq. (8) is generally valid for the topological surface state with a nonideal Dirac cone described by Eq. (1).

V. LANDAU-LEVEL FAN DIAGRAM FOR NONIDEAL DIRAC FERMIONS

Let us first consider how the LL fan diagram will be modified when both linear and parabolic terms are present in the Hamiltonian [Eq. (9)]. For the moment, the Zeeman coupling of the electron spin to the magnetic field is assumed to be negligible ($g_s = 0$). Figure 2(a) shows the calculated positions of maxima and minima in ρ_{xx} for oscillations with $F = 60$ T and $v_F = 3 \times 10^5$ m/s as m/m_0 is varied. One can see that upon decreasing m/m_0, the calculated lines on the LL fan diagram are gradually shifting upward from the ideal Dirac line that crosses the n axis at exactly $\frac{1}{2}$. Moreover, the lines are not straight anymore, which is reflected in the dependence of γ vs N shown in the inset. With decreasing N (increasing B), γ becomes larger, reflecting the change in the phase of oscillations at high fields.

A similar change in the LL fan diagram occurs if we modify another parameter, v_F. As shown in Fig. 2(b), the calculated lines are gradually shifting upward from the ideal Dirac line as

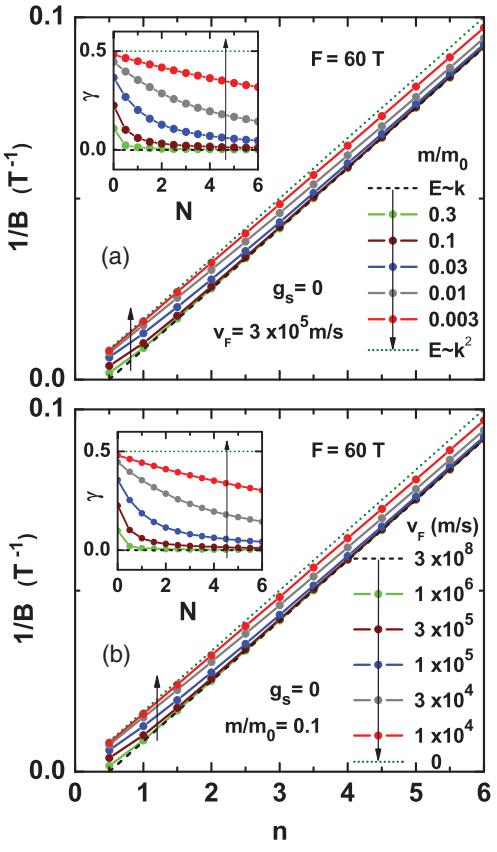

FIG. 2. (Color online) (a) Landau level fan diagram calculated for $F = 60$ T, $v_F = 3 \times 10^5$ m/s, $g_s = 0$, and different m/m_0. Arrows show the direction of decreasing m/m_0. The dashed and dotted lines are the expected behaviors for an ideal Dirac dispersion and a parabolic dispersion, respectively. (b) Landau level fan diagram calculated for $F = 60$ T, $m/m_0 = 0.1$, $g_s = 0$, and different v_F. Arrows show the direction of decreasing v_F. Insets show the calculated $\gamma(N)$.

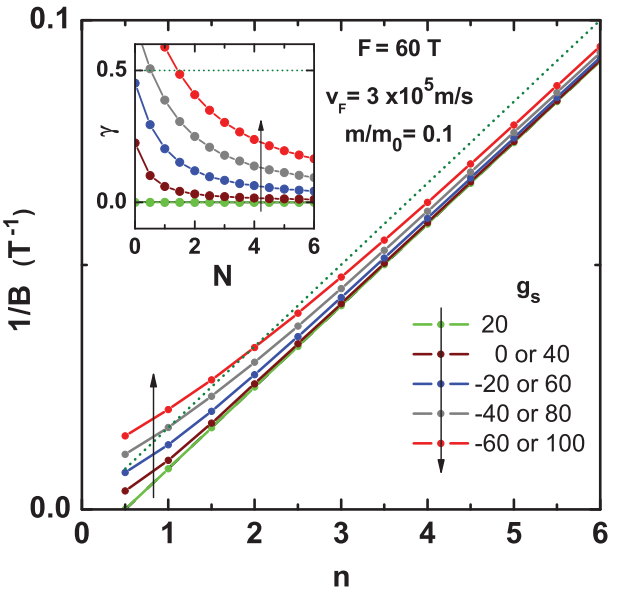

FIG. 3. (Color online) Landau-level fan diagram calculated for $F = 60$ T and different g_s, keeping $v_F = 3 \times 10^5$ m/s and $m/m_0 = 0.1$ constant. Arrows show the direction of changing g_s. The dotted line is the expected behavior for a parabolic dispersion. Inset shows the calculated $\gamma(N)$.

v_F is decreased. The results shown in Fig. 2 can be understood as a competition between linear and quadratic terms in the Hamiltonian [Eq. (9)]. Note that for the whole range of the parameters v_F and m/m_0, the positions of maxima and minima in ρ_{xx} lie between two straight lines (shown as dotted and dashed lines in Fig. 2) corresponding to $\gamma = 0$ and $\gamma = \frac{1}{2}$.

Let us now take the Zeeman term into consideration. Figure 3 shows the LL fan diagram calculated with $F = 60$ T, $v_F = 3 \times 10^5$ m/s, and $m/m_0 = 0.1$, while g_s is varied. To understand the effect of the Zeeman coupling, it is important to recognize the following two points: (i) The Zeeman term in Eq. (10) would tend to cancel the $\frac{1}{2}\hbar\omega_c$ term when g_s is positive. In fact, when $\frac{1}{2}\hbar\omega_c = \frac{1}{2}g_s\mu_B B$ (i.e., $g_s = 2m_0/m$) is satisfied, the effect of the finite effective mass is canceled and the LL fan diagram becomes identical to that for the linear dispersion (ideal Dirac) case. In the present simulations, we use $m/m_0 = 0.1$, so that this cancellations occurs when $g_s = 20$. (ii) A pair of g_s values that give the same $|\frac{1}{2}\hbar\omega_c - \frac{1}{2}g_s\mu_B B|$ are effectively the same in determining the behavior of the LL fan diagram. The result of our calculations shown in Fig. 3 is a demonstration of these two points. Since the Zeeman effect is more pronounced at higher fields, the LL fan diagram in Fig. 3 is strongly modified from a straight line when the quantum limit is approached, i.e., close to $N = 0$.

VI. THE CASE OF BTS

Let us examine the real data measured in the BTS sample,[21] in the light of the above considerations. Figure 4 shows the LL fan diagram for oscillations in $d\rho_{xx}/dB$ measured at $T = 1.6$ K in magnetic fields perpendicular to the (111) plane.[21] In Ref. 21, the data were simply fitted with a straight line, and the least-squares fitting gave a slope of $F = 64$ T with the intersection of the n axis at 0.22 ± 0.12; this result implies a

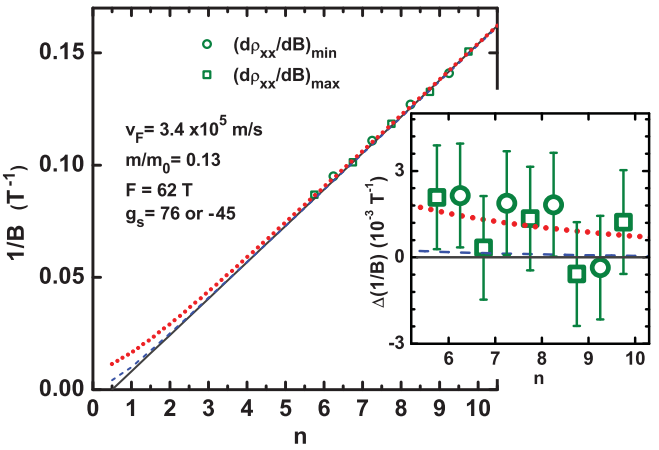

FIG. 4. (Color online) Landau-level fan diagram for oscillations in $d\rho_{xx}/dB$ measured at $T = 1.6$ K and $\theta \simeq 0^\circ$ reported in Ref. 21 for BTS. Minima and maxima in $d\rho_{xx}/dB$ correspond to $n + \frac{1}{4}$ and $n + \frac{3}{4}$, respectively. Solid (dark gray) line is the calculated diagram for an ideal Dirac cone with $v_F = 3.4 \times 10^5$ m/s and $F = 62$ T; dashed (blue) line includes the effect of the actual dispersion with $m/m_0 = 0.13$; dotted (red) line further includes the Zeeman effect, where $g_s = 76$ or -45 was determined from a least-squares fitting to the data. Inset shows the experimental data and calculations after subtracting the contribution from an ideal Dirac cone, $(1/B)_{\text{Dirac}}$, where $\Delta(1/B) \equiv (1/B) - (1/B)_{\text{Dirac}}$.

finite Berry phase, but it was not exactly equal to π, which remained a puzzle.[21] Now, we analyze this LL fan diagram by considering the nonideal Dirac dispersion as well as the Zeeman effect. The ARPES data[27] for the surface state of BTS (Fig. 1) give $v_F = 3.4 \times 10^5$ m/s and the averaged effective mass $m/m_0 = 0.13$. We fix the oscillation frequency F at 62 T obtained from the Fourier-transform analysis of the $d\rho_{xx}/dB$ oscillations.[21]

In Fig. 4, the calculated diagram for an ideal Dirac cone is shown by the solid (dark gray) line, whereas that for the nonideal Dirac cone with the effective-mass term is shown by the dashed (blue) line. One can see that the difference is small, which indicates that the effective mass of $0.13m_0$ is not light enough to significantly alter the LL fan diagram. One may also see that these two lines undershoot the actual data points at smaller n, which is even more clearly seen in the inset, where the experimental data and the calculations are shown after subtracting the contribution from an ideal Dirac cone. By further including the Zeeman effect, we can greatly improve the analysis, as shown by the dotted (red) line; here, g_s is taken as the only fitting parameter and a least-squares fitting to the data was performed. The best value of g_s is 76 or -45.

The inset of Fig. 4 makes it clear that it is the slight deviation of the experimental points from the ideal Dirac line that causes a simple straight-line fitting of the LL fan diagram to intersect the n axis not exactly at 0.5. Since the Berry phase in real situations is not a fixed value but is dependent on the magnetic field, the simple straight-line analysis of the LL fan diagram should not be employed for the determination of the Berry phase. Obviously, the SdH oscillations of the topological surface states are best understood by the analysis which considers both the the deviation of the energy spectrum

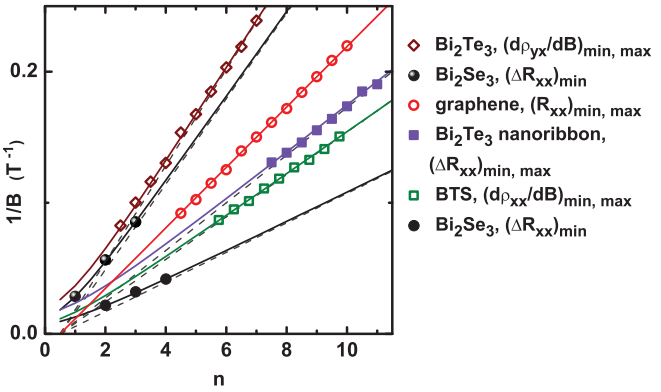

FIG. 5. (Color online) Landau-level fan diagrams for SdH oscillations observed in various TIs and graphene. Symbols are obtained from the published experimental data in the literature. Solid lines are calculations taking into account the nonideal dispersions of the surface states (determined by m/m_0) and the Zeeman coupling to an external magnetic field (determined by g_s). Dashed lines are calculations for ideal Dirac fermions ($m/m_0 = \infty$ and $g_s = 0$). Open diamonds are $(d\rho_{yx}/dB)_{\text{min,max}}$ in Bi_2Te_3 from Ref. 18; filled circles are $(\Delta R_{xx})_{\text{min}}$ in Bi_2Se_3 from Ref. 20; open circles are $(R_{xx})_{\text{min,max}}$ in graphene from Ref. 11; filled squares are $(\Delta R_{xx})_{\text{min,max}}$ in a Bi_2Te_3 nanoribbon from Ref. 25; open squares are $(d\rho_{xx}/dB)_{\text{min,max}}$ in BTS from Ref. 21.

of the Dirac-like charge carriers from the ideal linear dispersion and their strong coupling with an external magnetic field.

VII. OTHER MATERIALS

Similar analyses can be performed for other TIs in which the quantum oscillations coming from the 2D topological surface states have been observed. Figure 5 shows the LL fan diagrams for the SdH oscillations published to date for TI materials,[18,20,21,25,38] together with the data obtained in graphene,[11] which provides a good reference for studies of Dirac fermions. We digitized the published experimental data in the literature and determined ourselves the positions of minima $1/B_{\text{min}}$ and maxima $1/B_{\text{max}}$ of the oscillating parts of the resistivity (resistance), Hall resistivity, or their derivatives with respect to B. The data obtained for various materials are plotted as functions of n in Fig. 5. Note that, to avoid ambiguities, we considered only those data that show oscillations with a single frequency.[38]

The parameters of the surface states used in our fan-diagram analyses have been obtained from the published ARPES data by fitting them in the same way as for BTS (see Fig. 1). Table I shows v_F and m/m_0 for the Bi_2Se_3/Bi_2Te_3 family and graphene. These parameters were fixed during the fitting of the data shown in Fig. 5. The only parameter that could

TABLE I. Parameters of the surface states from ARPES.

Material	v_F (m/s)	m/m_0	Ref.	Remark
Bi_2Se_3	3.0×10^5	0.25	[28]	Averaged
Bi_2Te_2Se	3.4×10^5	0.13	[21]	Averaged
Bi_2Te_3	3.7×10^5	3.8	[29]	Near Dirac point
Graphene	1×10^6	∞	[11]	Calculations

TABLE II. Parameters used for the calculations shown in Fig. 5.

Material	Ref.	F (T)	E_F (eV)	g_s
Bi_2Se_3	[20]	30.7	0.074	55 or −39
Bi_2Se_3	[20]	88.6	0.143	55 or −39
Bi_2Te_2Se	[21]	62.0	0.152	76 or −45
Bi_2Te_3	[18]	27.3	0.074	65 or −65
Bi_2Te_3, nanoribbon	[25]	54.7	0.101	65 or −65
Graphene	[11]	43.3	0.239	0

vary in our calculations was g_s. Note that the frequency of oscillations F (and, thus, the Fermi energy E_F) is essentially determined by the periodicity of the observed oscillations. Table II summarizes the parameters thus obtained. The results of our calculations are shown in Fig. 5 by solid lines. Dashed lines depict the behavior expected for ideal Dirac cones ($m/m_0 = \infty$) and negligible Zeeman coupling ($g_s = 0$) for the TI data. One can clearly see in Fig. 5 that only graphene shows the ideal behavior in the LL fan diagram: a straight line that crosses the n axis at 0.5. All TI materials, despite their essentially Dirac-like nature of the surface state, present LL fan diagrams that deviate from the ideal behavior. (The deviations from the dashed lines are most clearly seen in strong magnetic fields.)

In view of the good agreements between the data and the fittings for all the materials analyzed in Fig. 5, one may conclude that the advanced analysis considering both the curvature of the Dirac cone and the Zeeman effect can reasonably describe the SdH oscillation data obtained for TIs and confirm the Dirac nature in their surface states.

VIII. SUMMARY

We derived the formula for the phase γ of the SdH oscillations coming from the surface Dirac fermions of realistic topological insulators with a nonideal dispersion given by Eq. (1). We also calculated how the curvature in the dispersion as well as the effect of Zeeman coupling affect the Landau-level fan diagram of the SdH oscillations for realistic parameters. Finally, we demonstrated that the Landau-level fan diagrams obtained from recently reported SdH oscillations in topological insulators can actually be understood to signify the essentially Dirac nature of the surface states, along with a relatively large Zeeman effect in those narrow-gap materials.

ACKNOWLEDGMENTS

We thank G. P. Mikitik for helpful discussions. This work was supported by JSPS (NEXT Program), MEXT (Innovative Area "Topological Quantum Phenomena" KAKENHI Grant No. 22103004), and AFOSR (AOARD Grant No. 10-4103).

[1] M. V. Berry, Proc. R. Soc. London, Ser. A **392**, 45 (1984).
[2] A. Shapere and F. Wilczek, *Geometrical Phase in Physics* (World Scientific, Singapore, 1989).
[3] R. D. King-Smith and David Vanderbilt, Phys. Rev. B **47**, 1651(R) (1993).
[4] D. Xiao, J. Shi, and Q. Niu, Phys. Rev. Lett. **95**, 137204 (2005).
[5] T. Thonhauser, D. Ceresoli, D. Vanderbilt, and R. Resta, Phys. Rev. Lett. **95**, 137205 (2005).
[6] N. Nagaosa, J. Sinova, S. Onoda, A. H. MacDonald, and N. P. Ong, Rev. Mod. Phys. **82**, 1539 (2010).
[7] J. Zak, Phys. Rev. Lett. **62**, 2747 (1989).
[8] D. Xiao, M. C. Chang, and Q. Niu, Rev. Mod. Phys. **82**, 1957 (2010).
[9] G. P. Mikitik and Yu.V. Sharlai, Phys. Rev. Lett. **82**, 2147 (1999).
[10] T. Ando, T. Nakanishi, and R. Saito, J. Phys. Soc. Jpn. **67**, 2857 (1998).
[11] K. S. Novoselov, A. K. Geim, S. V. Morozov, D. Jiang, M. I. Katsnelson, I. V. Grigorieva, S. V. Dubonos, and A. A. Firsov, Nature (London) **438**, 197 (2005).
[12] Y. Zhang, Y.-W. Tan, H. L. Stormer, and P. Kim, Nature (London) **438**, 201 (2005).
[13] L. Fu, C. L. Kane, and E. J. Mele, Phys. Rev. Lett. **98**, 106803 (2007).
[14] J. E. Moore and L. Balents, Phys. Rev. B **75**, 121306(R) (2007).
[15] R. Roy, Phys. Rev. B **79**, 195321 (2009).
[16] X.-L. Qi, T. L. Hughes, and S.-C. Zhang, Phys. Rev. B **78**, 195424 (2008).
[17] M. Z. Hasan and C. L. Kane, Rev. Mod. Phys. **82**, 3045 (2010).
[18] D.-X. Qu, Y. S. Hor, J. Xiong, R. J. Cava, and N. P. Ong, Science **329**, 821 (2010).
[19] A. A. Taskin, K. Segawa, and Y. Ando, Phys. Rev. B **82**, 121302(R) (2010).
[20] J. G. Analytis, R. D. McDonald, S. C. Riggs, J.-H. Chu, G. S. Boebinger, and I. R. Fisher, Nature Phys. **10**, 960 (2010).
[21] Z. Ren, A. A. Taskin, S. Sasaki, K. Segawa, and Y. Ando, Phys. Rev. B **82**, 241306(R) (2010).
[22] J. Xiong, A. C. Petersen, Dongxia Qu, R. J. Cava, and N. P. Ong, e-print arXiv:1101.1315.
[23] B. Sacépé, J. B. Oostinga, J. Li, A. Ubaldini, N. J. G. Couto, E. Giannini, and A. F. Morpurgo, e-print arXiv:1101.2352.
[24] C. Brüne, C. X. Liu, E. G. Novik, E. M. Hankiewicz, H. Buhmann, Y. L. Chen, X. L. Qi, Z. X. Shen, S. C. Zhang, and L. W. Molenkamp, Phys. Rev. Lett. **106**, 126803 (2011).
[25] F. Xiu, L. He, Y. Wang, L. Cheng, L.-T. Chang, M. Lang, G. Huang, X. Kou, Y. Zhou, X. Jiang, Z. Chen, J. Zou, A. Shailos, and K. L. Wang, Nature Nano. **6**, 216 (2011).
[26] D. Culcer, E. H. Hwang, T. D. Stanescu, and S. Das Sarma, Phys. Rev. B **82**, 155457 (2010).
[27] S. Y. Xu, L. A. Wray, Y. Xia, R. Shankar, A. Petersen, A. Fedorov, H. Lin, A. Bansil, Y. S. Hor, D. Grauer, R. J. Cava, and M. Z. Hasan, e-print arXiv:1007.5111v1.
[28] Y. Xia, D. Qian, D. Hsieh, L. Wray, A. Pal, H. Lin, A. Bansil, D. Grauer, Y. S. Hor, R. J. Cava, and M. Z. Hasan, Nature Phys. **5**, 398 (2009).

[29]Y. L. Chen, J. G. Analytis, J.-H. Chu, Z. K. Liu, S.-K. Mo, X. L. Qi, H. J. Zhang, D. H. Lu, X. Dai, Z. Fang, S. C. Zhang, I. R. Fisher, Z. Hussain, and Z.-X. Shen, Science **325**, 178 (2009).

[30]I. M. Lifshits and A. M. Kosevich, Zh. Eksp. Teor. Fiz. **29**, 730 (1955) [Sov. Phys. JETP **2**, 636 (1956)].

[31]E. Adams and T. Holstein, J. Phys. Chem. Solids **10**, 254 (1959).

[32]S. G. Sharapov, V. P. Gusynin, and H. Beck, Phys. Rev. B **69**, 075104 (2004).

[33]V. P. Gusynin and S. G. Sharapov, Phys. Rev. B **71**, 125124 (2005).

[34]D. Shoenberg, *Magnetic Oscillations in Metals* (Cambridge University Press, Cambridge, 1984).

[35]Z. Wang, Z.-G. Fu, S.-X. Wang, and P. Zhang, Phys. Rev. B **82**, 085429 (2010).

[36]Y. A. Bychkov and E. I. Rashba, Pis'ma Zh. Eksp. Teor. Fiz. **39**, 66 (1984) [JETP Lett. **39**, 78 (1984)].

[37]B. Seradjeh, J. Wu, and P. Phillips, Phys. Rev. Lett. **103**, 136803 (2009).

[38]We did not include the data reported in Refs. 19 and 24, because the SdH oscillations observed in $Bi_{0.91}Sb_{0.09}$ (Ref. 19) and in a strained epitaxial film of HgTe (Ref. 24) clearly show multiple frequencies.